Anisotropic magnetic properties of bi-layered structure of ordered Co nanorod array: micromagnetic simulation and experiments

P. D. Kulkarni, B. Sellarajan, M. Krishnan, Harish C. Barshilia, and P. Chowdhury
Surface Engineering Division, National Aerospace Laboratories,
Council of Scientific and Industrial Research, Bangalore-560 017, India

The angular dependence of magnetic properties were investigated in Co nanowire (NW) arrays with varying length grown by pulse electrochemical route into pore of alumina template. In these investigations, three different NW lengths, 200 nm , 400 nm and 1000 nm were considered. The structural investigations reveals that shorter NW of length 200 nm have hcp (002) structure, however the existence of both hcp (002) and hcp (100) was observed in longer wire length of 1000 nm, though these phases were well separated in lower and upper segments along the NW axis, respectively. Micromagnetic simulation has been carried out considering the different crystallographic structures as a function of NW length and with the variation of angle between the applied field and the NW axis. Both using experimentally measured magnetization data and micromagnetic simulations, we have inferred that in the nanowire with only hcp (002) structure, the magnetization reversal occurs by coherent rotation, whereas in the case of hcp (100) structure, the reversal phenomena occurs via vortex state and in bilayer structure, the interaction among them leads to a gradual crossover from a coherenet state to vortex along the nanowire axis. Irrespective of the NW length, the angular dependence of H_c was explained qualitatively using the micromagnetic simulation.

I. INTRODUCTION

Recently, the physics of magnetic nanowire (NW) arrays have attracted great attention due to easy accessible route of electrochemical deposition through anodic aluminum oxide (AAO) template[1]. Main advantages in this bottom-up technique are: (i) AAO template can be fabricated with varying pore diameter, length and periodicity, by simple changing the processing parameters, such as anodising voltage, electrolyte and electrolyte temperature[2, 3] and (ii) the crystalline properties of fabricated NWs can be tuned by adjusting the electroplating conditions, such as, pH, plating current and bath temperature[4–7]. Hence, through this route, magnetic NW arrays of Ni, Co, Fe and their alloys were fabricated and extensive investigations both on the structural and magnetic properties were reported[8, 9].

Though, most of the structural investigations on electrodeposited Co NWs were observed to have polycrystalline in nature[10], textured growth of Co NW arrays with hcp phase was reported recently[6, 7, 11, 12]. The crystalline orientation with respect to the NW axis influences the magnetic anisotropy in many ways[9, 13]. In 1-D magnetic NWs, two major contributions, namely; the shape anisotropy and the magnetocrstalline anistropy, determine the basic properties of system. The shape anisotropy is controlled by the demagnetization factor (N_z) and this results from the ratio of longitudinal (L) to lateral dimension (D). With larger aspect ratio (L/D), the shape anisotropy enhances the effective longitudinal anisotropy. However, the magnetocrystalline anisotropy, originated from the crystalline structure of the materials, modifies the effective anisotropy in the system. For an example, in hcp Co phase, the magnetization easy axis, originated from the magnetocrystalline anisotropy, lies along the direction of crystallographic c-axis. Therefore, in Co NWs grown with hcp (002) phase, the magnetocrystalline anisotropy enhances the longitudinal anisotropy, whereas in the case of hcp (100), this reduces the effective anisotropy. NWs grown with a bi-layer structure of two different hcp phases mentioned above have a competitive magnetocrystalline anisotropies, which will greatly modify the reversal magnetization process.

For better understanding the reversal magnetization behavior in magnetic NW arrays, the angular dependence of magnetization with respect to the wire axis was reported to be an useful tool[1, 14–18]. Theoretically, the magnetization reversal process of a NW with given anisotropy was explained by three different modes, namely: coherent rotation (C) in which all the spins rotate simultaneously; transverse rotation (T) in which spins rotation takes place via propagation of transverse domain wall; and curling or vortex rotation (V), in which spins are reversing their directions via propagation of vortex domain wall. Analytical formula of each mechanism for single NW was well established through angular dependence of the nucleation field, H_n, as this field is directly co-related with the reversal mechanism. Irrespective of the NW crystallographic structure, the experimental results for $H_n(\theta)$ with large aspect ratio ($>$ 50) were explained with transverse mode. Recently, micromagnetic simulation along with experimental data revealed that the existence of different spin configurations (i.e. coherent or vortex) depending on the NW crystallographic structure where the transverse mode cannot be applied[11, 12]. Therefore, the applicability of these models for NW array is ruled out because of: (i) the existence of long range dipolar interactions among NWs, and (ii) bi-layer structures with different crystallographic orientations. On the other hand, micromagnetic simulation was found to be very powerfull technique to understand the reversal mechanism on complicated structures.

In this work, we have investigated the magnetic prop-

erties of ordered Co NW arrays with three different wire lengths having different crystallographic structures. The variation of measured angular dependance of coercive field was then correlated with the simulated data calculated using micromagnetic simulation. From these correlation, we have inferred that in the shorter NWs of length L≤300 nm with hcp (002) structure, the magnetization reversal occurs by coherent rotation, whereas in the longer NWs the existence of both hcp (002) (lower segment) and (100) (upper segment) complicates the reversal process.

II. EXPERIMENTS:

Ferromagnetic nanowire arrays were prepared by pulse eletrodeposition of Co^{2+} metal ions into the pores of alumina template of thickness $\sim$ 12 μm. AAO was prepared by a two-step anodization process and described elsewhere[12, 21, 22]. In order to investigate the magnetic anisotropic behavior of 1-D Co NW arrays with varying aspect ratio, the length of the NW from 100 to 4000 nm was controlled by the number of cycles during the deposition. The wires grew in the usual bottom-up fashion starting from the Ag electrode at the pore bottoms. Electro-deposition was carried out using an aqueous electrolyte containing 120 g/l $CoSO_4$ and 50 g/l H_3BO_3 at room temperature with pH $\sim$ 2.8. The pulse deposition was carried out with T_{on} = 20 ms and T_{off}= 20 ms and the pulse height was -2 V[10]. The details regarding the electrodepostion conditions for this material was described in our previous paper[12]. Morphological and structural characterizations of samples were performed using a Zeiss Supra 40 VP field emission scanning electron microscopy and a Burker D8 Advanced X-ray diffractometer (XRD), respectively. Angular dependence study on the magnetic properties of the nanowire arrays at room temperature was carried out by a vibrating sample magnetometer (VSM, Lakeshore). Micro-magnetic simulations were carried out to investigate the micromagnetic properties of the magnetic nanowires by using three-dimensional (3D) object oriented micro-magnetic frame work (OOMMF).

III. THEORY:

Most of earlier studies of angular dependence of magnetic anisotropy in 1D system were based on analytical formulae given in Ref. [18]. As mentioned above, these theories can be applied to a uniaxial system with non-interacting media. Secondly, these formulae do not include the effect of crystallographic structure on magnetic properties. Therefore, we have used micromagnetic simulation to understand the reversal mechanism in 1D system with different crystallographic structures as well as their combined bi-layer structure. To establish the correlation between the structural investigations with observed angular magnetic behaviors, we have performed the micromagnetic simulation using the 3D-OOMMF package[7, 23] with varying the external field direction at different angles with respect to the the NW axis. To perform the simulation using this package, the real structure of the system was decomposed with regular 3D square meshes with each mesh containing 3D magnetization spin vector located at the center of the cell. In the simulation, the magnetization distribution in the system was then evaluated by integrating the Landau-Lifshitz equation:

$$\frac{d\mathbf{M}}{dt} = -\gamma \mathbf{M} \times \mathbf{H}_{eff} - \frac{\gamma\alpha}{M_s} \times (M \times \mathbf{H}_{eff}), \quad (1)$$

where
M is the magnetization of each 3D mesh,
H_{eff} is the effective field of the mesh,
γ is the gyromagnetic ratio,
α is the damping coefficient.
The effective field is defined as:

$$\mathbf{H}_{eff} = \frac{1}{\mu_0} \frac{\partial E_{total}}{\partial \mathbf{M}}. \quad (2)$$

The average magnetic energy density, E_{total} is the addition of the four different magnetic energy contributions as follows:
(i) the magnetostatic energy, E_m, arises due the interaction of the magnetization $\mathbf{M}$ with the demagnetising field, $\mathbf{H}_d$, which is proportional to induced $\mathbf{M}$ and is defined as[12]:

$$E_m = -\mu_0 \mathbf{H}_d \cdot \mathbf{M}/2, \quad (3)$$

(ii) the magnetocrystalline anisotropy energy, E_{an}, arises due to the magneto-crystalline anisotropy of the system and can be written as:

$$E_{an} = K_1 sin^2\psi, \quad (4)$$

where ψ is the angle between the easy axis and the magnetization $\mathbf{M}$, and K_1 is the anistropy constant,
(iii) the exchange energy, E_{ex}, originates from the misalignment of a spin with respect to the neighbouring spin and can be written as:

$$E_{ex} = A \sum_{i=1}^{3} (\Delta M_i)^2/(M_s)^2, \quad (5)$$

and (iv) the Zeeman energy in presence of the external field $\mathbf{H}$, is defined as:

$$E_{ze} = -\mathbf{M} \cdot \mathbf{H}. \quad (6)$$

It is to be mentioned that in case of NW arrays, Eqn.(3) for E_m gets modified as $E_m = -\mu_0(\mathbf{H}_d + \mathbf{H}_{dp}).\mathbf{M}/2$, where $\mathbf{H}_{dp}$ is the dipolar interaction field arising due to interaction between neighboring NWs.

The analytical formula to determine the angular dependence of the nucleation for coherent reversal mechanism was derived by Stoner-Wohlfarth and can be written as[24]:

$$H_n^C(\theta) = -\frac{2[K_{sh}(L_{nw}) + K_{mc}]\sqrt{1-t^2+t^4}}{\mu_o M_s^2(1+t^2)} M_s. \quad (7)$$

Here $t = \tan^{1/3}(\theta)$, with θ is the angle between the field and NW cylindrical axis, M_s is the saturation magnetization, $K_{sh}(L_{nw})$ is the shape anisotropy constant and K_{mc} is magnetocrystalline anisotropy constant. Further $K_{sh}(L_{nw})$ can be written as:

$$K_{sh}(L_{nw}) = \frac{1}{4}\mu_o M_s^2[1 - 3N_z(L_{nw})], \quad (8)$$

with $N_z(L_{nw})$ as demagnetization factor along the z-axis and can be determined using the relation;

$$N_z(l) = 1 - F_{21}[2D^2/L^2) + \frac{4D}{3\pi L} \quad (9)$$

where, $F_{21}(y)$= F_{21}[-1/2,1/2,2,-y] is a hypergeometric function.

For NWs with higher lengths the coherent rotation is found to be less favorable energetically. In such cases the revarsal mechanism can happen by transverse rotation by domain wall propagation. Assuming that for magnetization reversal by means of nucleation and propagation of a transverse wall the field is equal to nucleation field of an equivalent system with an effective volume that reverses its magnetization by coherent rotation, Escrig *etal*. had calculated the equation for nucleation field, H_n^T, as[16]:

$$H_n^T(\theta) = -\frac{2[K_{sh}(\omega_T) + K_{mc}]\sqrt{1-t^2+t^4}}{\mu_o M_s^2(1+t^2)} M_s, \quad (10)$$

where

$$K_{sh}(L) = \frac{1}{4}\mu_o M_s^2[1 - 3N_z(\omega_T)], \quad (11)$$

with ω_T as domain wall. is In general, ω_T is taken to be 50 nm more than NW diameter (or almost double than D? i.e. for D=35-50nm w_T = D+ 50. Then for D=70nm W_T = D+70 to 90?). Hence, For NWs with length L >> ω_T the reversal takes place by transverse mode and for L $\sim \omega$ reversal takes place by coherent mode.

IV. RESULTS AND DISCUSSION

Figure 1(a) show the FESEM image of AAO membrane with hexagonal pore arrays. The average diameter and interpore distance are estimated as 70±5 nm and 90±5 nm, respectively. The cross sectional views of AAO mambrane with partially filled Co NWs with two different wire lengths, 200 and 400 nm are shown in Fig. 1(b) and (c) respectively.

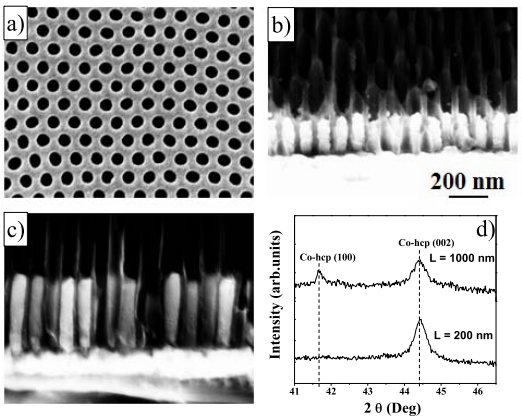

FIG. 1. FESEM images of AAO membrane (a) top view, cross-sectional view filled with Co nanowires with (b)$L = 200$ nm and (c)$L = 400$ nm. (d) X-ray diffraction patterns of Co nanowires with varying L of the nanowires.

Figure 1(d) presents the XRD patterns for NWs for L = 200 and 1000 nm. As shown in this figure, only one peak is observed at $2\theta = 44.4^o$ for the NW array with L = 200 nm, indicating textured growth of Co hcp (002) structure. Interestingly, with increase in length to L = 1000 nm of the NWs, one more peak corresponding to Co hcp (100) appears at $2\theta = 41.6^o$ along with the existing hcp (002) peak. The detailed structural investigations as a function of wire length were reported earlier[12]. In that report along with micromagnetic simulation, it was clearly shown that initially Co grows into the pores with hcp (002) texture up to 300 nanometers and then the growth orientation changes to hcp (100) as L increases. It is to be mentioned that there might be an existence of an intermediate region of width 200 nm where the mix state of both textures lies.

Figures 2(a)- 2(c) presents the M-H hysteresis curves measured for the NW arrays with three different L values; 200, 400, and 1000 nm, respectively. M(H) data presented here, are measured with varying the angle, θ, between 0^o to 90^o. Here, θ is the angle between the applied field, H, and NW axis. Irrespective of the NWs length, M(H) curves show systematic decrease in hysteresis loops with increasing θ from 0^o to 90^o and M_r/M_S follows the cosine function of this angle as expected. This indicates that the bulk easy axis arising from both the shape and magnetocrystalline anisotropies lies along the NWs axis. However, the anisotropy field, H_k (= $H_s^{90^o} - H_s^{0^o}$, H_s is the saturation field), decreases with the increasing length of the NWs, indicating a transformation from an anisotropic to isotropic system. The variation of H_c as function of θ for three different wire lengths is shown in Fig 2(d). It is interesting to see that irrespective of the nanowire length, H_c decreases sharply for $\theta > 45^o$. However for $\theta < 45^o$, for NW of length 200 nm, the values of H_c are independent of the angle, whereas for $L = 400$ nm, an increasing trend in H_c was observed and for $L =$

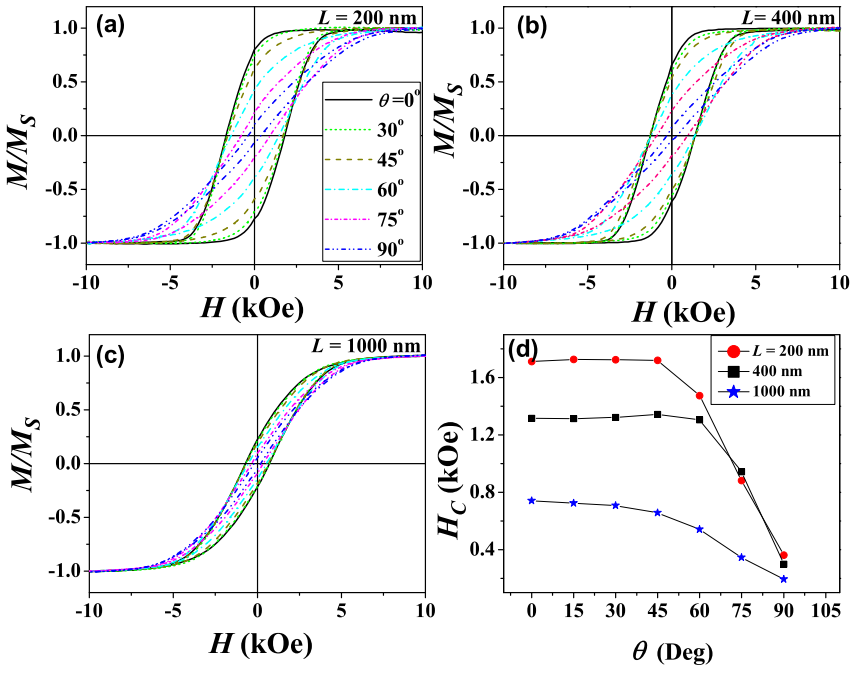

h

FIG. 2. Measured M(H) loops of Co nanowire arrays for lengths (a) 200 nm, (b) 400 nm, and (c) 1000 nm with varying θ. (d) shows the measured H_c and as a function of angle θ.

1000 nm, H_c was found to decrease slowly.

To understand the experimentally observed angular dependence of $H_c(\theta)$ for three different wire lengths, the simulations were performed on three different structures as defined below. For the NWs, with L = 200 nm, the structure was considered to be hcp (002) with the crystallographic c-axis in longitudinal direction. For L = 400 nm, the texture is defined as two segments along the NW length; the lower segment of length 300 nm with hcp (002) structure and a mixture of hcp (002) and (100) with equal percentage for the upper segment. While simulating for L = 1000 nm, we have considered thrre diiferent segments: (i) lower segment of length 300 nm with hcp (002) texture, (iii) middle segment of length 200 nm with mixed structure of both hcp (002) and hcp (100), and (iii) upper segment of length 500 nm with hcp (100) structure. It is to be mentioned that the simulations were performed on single NW as well as hexagonal ordered array of seven NWs. In case of NW array with individual wire length of 200 nm, the simulation was also performed on a hexagonal ordered array of maximum 72 (8 × 9 matrix) NWs based on the computational facilities currently available. Here, in the simulation, the radius, r, was taken as 35 nm. In the case of hexagonal ordered array structure, the centers of NW axes were kept at a separation, s = 90 nm. We have considered the parameters of bulk Co, as $A = 1.3 \times 10^{-11}$ J/m (the exchange constant), M_S =1.76 T (the saturation magnetization), and $K_1 = 5.2 \times 10^5$ J/m^3 (magneto-crystalline anisotropy constant of a Co hcp phase).

Fig 3 (a) -3(c) presents the simulated $M(H)$ curves for three different wire lengths, 200, 400 and 1000 nm, respectively with hexagonal ordered array of seven NWs. M(H) curves presented here, are simulated with varying the applied field angles, θ, between 0^o to 90^o with respect to the NW axis. Similar to the experimental results (see Fig 2(a)-2(c)), $M(H)$ curves show systematic decrease in hysteresis loops with increasing θ. The variation of H_c as a function of θ for three different wire lengths are shown in Fig 3(d). It is interesting to see that the behavior of H_c for L = 200 and 400 nm are similar to those for experimental ones (see Fig. 2(d)). However, the coercivity values extracted from the simulated curves are almost two times larger than the experimental values. On the other hand, the corecivity values in case of L = 1000 nm, are very close to the experimental one. To understand the large discrepancy in H_c for shorter wire lengths, one has to look into the magnetic moment distribution across the NW length arising due to different crystallographic structure.

For the NW with hcp (002) texture (i.e., L = 200 nm), both the shape and the magnetocrystalline anisotropies refer same easy axis along the z-direction. This leads to a coherent state at the remanence with all the spins direction parallel to the easy axis (see Fig 4 (a)). Therefore, in this system, M_r/M_s becomes one and the demagnetizing field, $H_d = N_z M_s$ becomes maximum. In the NW array structures, along with H_d, antiferromagnetic cou-

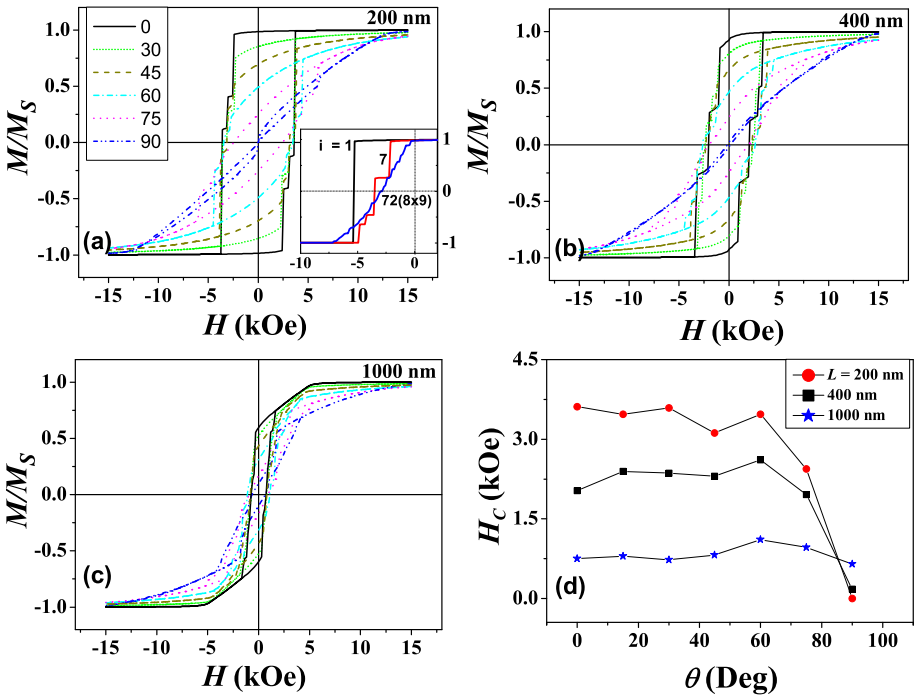

FIG. 3. Simulated M(H) curves as a function of θ for (a) L = 200 nm, (b) L = 400 nm (c) L = 1000 nm. The nanowire structure used for simulations is as given in explanation. Inset of (a) shows shearing of M(H) curve with increase in no. of nanowires. (d) Simulated H_c vs θ for different nanowire lengths.

pling between the neighboring NW gives rise to a dipole interaction field, H_{dp}, which depends on both the length, L and separation, s among the NWs. The dipolar interaction field effectively reduces the corecivity. This can be understood from the simulations by changing the number of NWs in an array. The simulated $M(H)$ data for a single NW is perfectly rectangular (see inset fig. 3 (a)). As the number increases to seven NWs in a hexagon array, the magnetic reversal happens in steps suggesting individual NW reverses coherently at different external fields, H_C^i, which can be defined as[16],

$$H_C^i = H_C^s - H_{int}, \tag{12}$$

where H_C^s is the coercive field of a single NW. Here i stands for the number of nanowires in the array. The sign of H_{int} can be negative or positive, however its magnitude depends on the location and separation with respect to the neighboring NWs and their magnetization directions. For an example, H_{int} is maximum when all the NWs in a array have their magnetization directions parallel to each other (i.e., M = M_s). Reversing a nanowire at a field much lower than H_C^s followed by Eqn. (12), effectively reduces H_{int} which is nothing but the step width between successive Barkhausen jumps. With further increase in the number of NWs in the array structure, the M(H) behavior ends with a sheared behavior (see inset Fig. 3 (a) for 8×9 NW array) due to increase in the number of Barkhausen junps. This figure, also indicates that H_c was found to decrease by 50 % with increase in the number of NWs from single NW to an array of 8×9 NWs. This explains why the large discrepancy was observed in H_c between the experimental and simulated one. Along with number of nanowires, one need to consider the other factors, such as defects, physical shape variations among the NWs, to match with the experimental H_c values with theory. Fig 4 (b) presents the variation of H_c as a function of angle calculated using analytical formula (Eqn. (7)) along with the extracted H_c variation obtained from the micromagnetic simulations for single NW a well as seven NWs in a hexagon array. It is interesting to see that the functional form of $H_c(\theta)$ calculated from the analytical formula is matching well with that obtained from single NW simulation as expected. From these observations, we conclude that in hcp (002) structure, the reversal mechanism occurs only by coherent rotation of the magnetic moment vectors, not by transverse mode as reported earlier[1], as our NWs have smaller aspect ratio (< 3).

To understand the reversal mechanism for NWs with L = 400 and 1000 nm, it is necessary to clear the picture of magnetic state in a NW with hcp (100) structure. The remanent magnetic state of a NW with hcp (100) structure was characterized by a vortex state with opposite chiralities separated by domain wall of width around 100 nm (see Fig. 5(a)). The magnetization in this state can

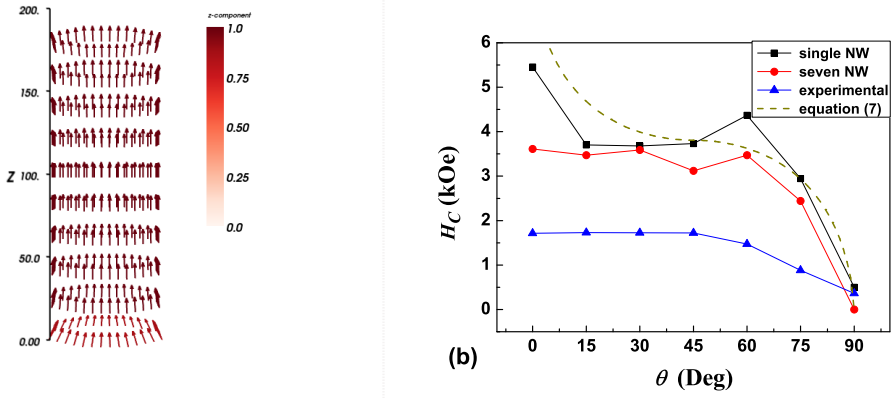

FIG. 4. (a)Nanowire cylinder at remnant state for L = 200nm with hcp (002) structure showing the magnetic spins parallel to NW axis indicating single domain. (b) Comparison of H_c vs θ curves in case of NW with L = 200nm showing effect of interaction among the nanowires on H_c.

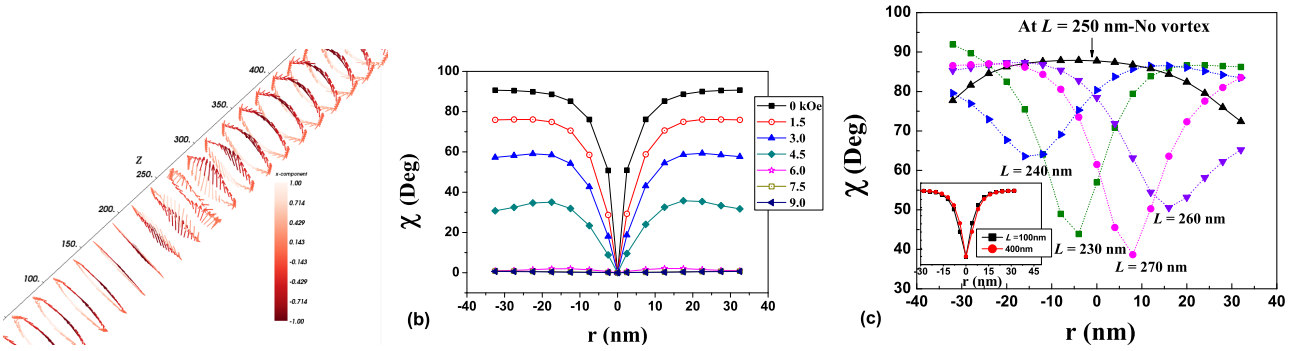

FIG. 5. (a) Nanowire cylinder of L = 500 nm with hcp (100) structure at remnant state showing two vortices (clockwise and anti-clickwise) **merging** at center. (b) χ vs r at middle of NW. No vortex at L = 250 nm. (c) χ vs r showing decrease in vortex intensity with increasing H.

be expressed as[12, 25–27]:

$$\mathbf{M} = \sum_N (M_s \cos\chi_i \hat{z} + M_s \sin\chi_i \hat{\varphi}), \qquad (13)$$

where χ_i is the angle between **M** and the NW axis or $\hat{z}$ of the i^{th} element. Fig. 5 (b) presents the angular distribution of **M** along the radial direction with respect to the NW axis, i.e., χ, at the remanence state for different z values. As shown in this figure (inset of Fig. 5 (b)), for z =100 and 400, χ changes from 90^o to 0^o along the radial direction as one approaches towards center. This implies that along the $\hat{z}$ direction for a constant (r,φ), χ remains unchanged. Therefore, a solid NW with hcp (100) structure can be defined as parallel cylindrical shells with constant **M** (See Fig. 5 (a)), however at the middle, the cylinder is twisted to form a domain. As shown in Fig 5 (b), the domain also can be characterized by a vortex state (Eqn. (13)) for which the center of the vortex is shifted towards the edge (-ve r direction) with clockwise rotation as $\hat{z}$ approaches $L/2$ and vanishes completely exactly at $z = L/2 = 250$ nm. Further increasing z, vortex starts appearing on the other side (+ve r direction) with anti-clockwise rotation and then moved towards the center. For further understanding the reversal mechanism, the radial distribution of χ with increasing the field from 0 (remanence state) to the saturation field is shown in Fig 5 (c). Here the field was applied along the $\hat{z}$ direction. From this figure it is clear that the intensity of vorticity (i.e. the angular distribution of **M**) is high at the remanence state and it decreases with the increasing field, and vanishes at the saturation field. Therefore, we can conclude that in pure hcp (100) structure, the reversal mechanism occurs via a process with reducing the vorticity along with the domian wall motion which creates at two ends and annihilate at the center of the NW.

At the remanence state, the distribution of z-component of **M** for the NW of length 1000 nm is shown in Fig 6(a). In this figure, the distribution is shown only for outer cylindrical shell for better clarity, though the actual simulations are carried out on a solid cylinder. Three planar sections with M_z component for three dif-

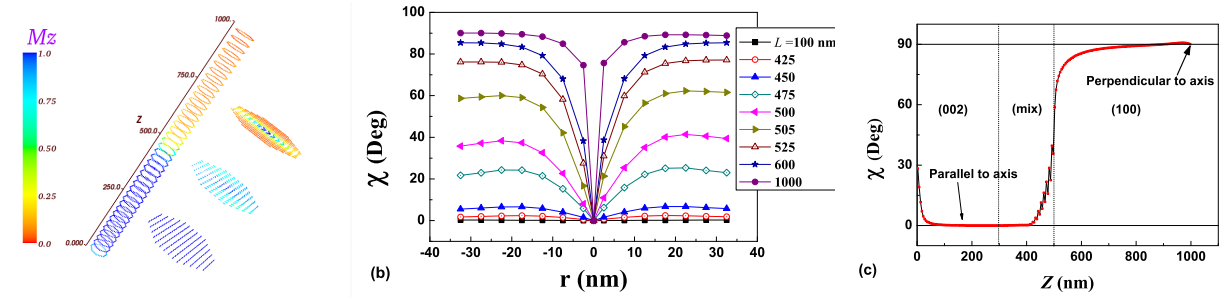

FIG. 6. (a) Nanowire cylinder of L = 1000 nm with hcp (002) and (100) structures (see text) at remnant state. (b) variation in χ with L showing coherent domain at lower thickness and appearance of vortex for L > 400 nm. (c) Variation in χ with L indicating interaction region.

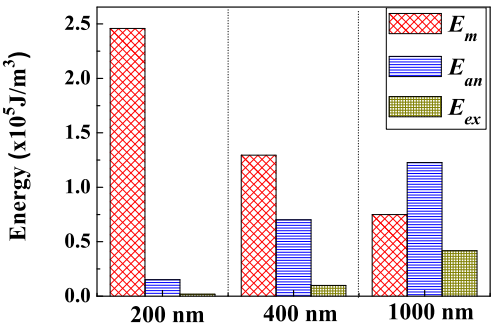

FIG. 7. Different energy contributions in three cases of L = 200 nm, 400 nm and 1000 nm at remnant state.

ferent z-values are shown in the same figure. From these views, we can infer that NW of length 1000 nm with three segments have following magnetic moment distributions; (i) lower segment of length 300 nm with hcp (002) structure shows that moment vectors are aligned parallel to each other and to the z-axis, i.e., NW axis and it known as a coherent state, (ii) middle segment of length 200 nm with equal percentage of hcp (002) and (100) structures shows a gradual change from coherent to vortex state, and (iii) upper segment of length 500 nm with hcp (100) structure shows a dominant magnetic vortex state. Fig 6 (b) presents χ along the radial direction for different z-values. This figure clearly indicates that whole length of NW can be divided into two segments with respect to the the magnetic state. First a lower segments of length 400 nm dominated by coherent state. Then With further increasing the z value vortex starts appearing and the intensity of the vorticity increases with increasing length and reaches to 90% of its maximum value at a length of 600 nm (see figure 6 (c)). These results imply that a mix state with equal percentage of hcp (100) and hcp (002) structures can be represented by gradual crossover from a coherent state to a vortex state. Interestingly, in the upper segment of this bilayer structure no domain was formed as observed in the case of single hcp (100) structure (Fig 5(a)).

It is equally important to see the change of different energy density contributions defined by Eqs. (3-6) while NW growing in length. Fig. 7 presents the energy density (J/m^3) bar diagram of different energy contributions at remanent state for NW length L = 200, 400, and 1000 nm, respectively. Since in all three cases external field H = 0, Zeeman energy E_{ze} is not considered. For L = 200 nm, with hcp (002) structure, spins are aligned parallel to each other (i.e., coherent state) with $\psi = 0$, therefore, the anisotropy energy, E_{an} and the exchange energy, E_{ex} both become negligible. But the magnetostatic energy, $E_m \sim 2.45\times10^5$ J/m^3, is more than that of 400 nm and 1000 nm and is dominant over all other energies. This dominance of E_m gives better squareness ($M_r/M_S = 1$) in 200 nm with highest H_c as can be seen in Fig. 3. In case of L = 400 nm, as explained earlier, the structure represents 100 nm mix region on the top of 300 nm hcp (002). This provides 15 % volume contribution of hcp (100) structure in the whole 400 nm length. But interestingly, it decreases E_m by almost 50 % to 1.3×10^5 J/m^3 as spins in mix region start curling, loosing the perfect coherent structure. This can be seen as E_{ex} starts appearing ($\sim 9.9\times10^3$ J/m^3) along with increased E_{an} ($\sim 0.7\times10^5$ J/m^3). The effect of this can be seen in a decrease in H_n (and hence in H_c) for 400 nm than that of 200 nm. It has to be mentioned here that, though the curling of spins started, the magnetization reversal is still dominated by coherent rotation as $M_r/M_s \sim 1$. For NWs with L = 1000 nm, hcp (100) dominates the structure. This gives highest E_{an} ($\sim 1.3\times10^5$ J/m^3) among all three cases. Apart from that, E_{an} is most dominant in all energy contributions in 1000 nm as hcp (100) structure has easy axis of magnetocrystalline anisotropy perpendicular to wire axis giving $\phi = 90^o$. A single vortex appears in 1000 nm as explained earlier, which enhances E_{ex} to its maximum value in all three NWs ($\sim 0.43\times10^5$ J/m^3).

V. CONCLUSION

In conclusion, we have studied both the structural and the angular properties of electrodeposited Co NWs with varying the NW length. The observed magnetic properties were then explained with the help of micromagnetic simulations and it was shown that the Co texture plays an important role in defining the magnetic properties in NWs. In shorter wire length with hcp (002) structure, the reversal occurs via coherent process, whereas in longer one with existing of both hcp (002) and hcp (100) structure, a gradual crossover from a coherent state at lower segment to vortex state at upper segment was observed. It was also shown that in a array with hcp (002) structures, the dipole interactions among them effectively reduces the coercivity in the system by 50%. Moreover, with addition of small percentage (15%) of hcp (100) structure at the top of the NW, the magnetostatic energy arising due to dipolar interaction decreases dramatically, which in turn reduces H_c by 50% keeping squareness ratio almost one. This might be due to initiation of the vortex state at one end of the nanowire. With further addition of hcp (100) structure, the anisotropy field (H_K) was found to decrease, indicating a decrease in uniaxial anisotropy in the system. Thus, by controlling the bilayer lengths of hcp (002) and (100) in Co NWs, it can be possible to control the magnetic properties, such as, H_c, squareness ratio, magnetic anisotropy. Therefore, these studies are very important to understand the physics of magnetic states towards the memory applications where the magnetic arrays with higher effective longitudinal anisotropy, lower H_c and reduced interaction are required.

ACKNOWLEDGMENTS

Authors would like to thank the Director, NAL for supporting this activity.

[1] L. G. Vivas, J. Escrig, D. G. Trabada, G. A. Badini-Confalonieri, and M. Vzquez, Appl. Phys. Lett. **100**, 252405 (2012).

[2] K Nielsch, J Choi, K Schwirn, Ralf B. Wehrspohn, and U Gosele, Nano Lett., **2(7)**, 677 (2002).

[3] A. P. Li, F. Muller, A. Birner, K. Nielsch, and U. Gosele, J. Vac. Sci. Technol. A **17(4)**, 1428 (1999).

[4] M. Darques, A. Encinas, L. Vila, and L. Piraux, J. Phys.: Condens. Matter **16**, S2279 (2004).

[5] X. W. Wang, G. T. Fei, P. Tong, X. J. Xu, and L. D. Zhang, Journal of Crystal Growth **300**, 421 (2007).

[6] X Han, Q Liu, J Wang, S Li, Y Ren, R Liu, and F Li, J. Phys. D: Appl. Phys. **42**, 095005 (2009).

[7] Y. Ren, J. Wang, Q. Liu, Y. Dai, B. Zhang, and L. Yan, J. Mater. Sci. **46**, 7545 (2011).

[8] H. Pan, B. Liu, J. Yi, C. Poh, S. Lim, J. Ding, Y. Feng, C. H. A. Huan, and J. Lin, J. Phys. Chem. B **109**, 3094 (2005).

[9] G. Kartopu, O. Yalçin, M. Es-Souni, and A. C. Başaran, J. Appl. Phys. **103**, 093915 (2008).

[10] J. Zhang, Grenville A. Jones, Tiehan H. Shen, and Steve E. Donnelly, and G. Li, J. Appl. Phys. **101**, 054310 (2007).

[11] L. G. Vivas, R. Yanes, O. Chubykalo-Fesenko, and M. Vazquez, Appl. Phys. Lett. **98**, 232507 (2011).

[12] B. Sellarajan, P. D. Kulkarni, M. Krishnan, Harish C. Barshilia, and P. Chowdhury, Appl. Phys. Lett. **102**, 122401 (2013).

[13] J. Sánchez-Barriga, M. Lucas, F. Radu, E. Martin, M. Multigner, P. Marin, A. Hernando, and G. Rivero, Phys. Rev. B **80**, 184424 (2009).

[14] G. C. Han, B. Y. Zong, P. Luo and Y. H. Wu, J. Appl. Phys. **93**, 9202 (2003).

[15] P. Landeros, S. Allende, J. Escrig, E. Salcedo, D. Altbir, and E. E. Vogel, Appl. Phys. Lett. **90**, 102501 (2007).

[16] J. Escrig, J. Bachmann, J. Jing, M. Daub, D. Altbir, and K. Nielsch, Phys. Rev. B **77**, 214421 (2008).

[17] R. Lavin, J. C. Denardin, J. Escrig, D. Altbir, A. Cortés, and H. Gómez, J. Appl. Phys. **106**, 103903 (2009).

[18] L. G. Vivas, M. Vazquez, J. Escrig, S. Allende, D. Altbir, D. C. Leitao, and J. P. Araujo, Phys. Rev. B **85**, 035439 (2012).

[19] F. Li, L. Zhang, and R. M. Metzger, Chem. Mater. **10**, 2470 (1998).

[20] S. K. Hwang, S. H. Jeong, H. Y. Hwang, O. J. Lee, and K. H. Lee, Korean J. Chem. Eng. **19(3)**, 467 (2002).

[21] P. Chowdhury, K. Raghuvaran, M. Krishnan, Harish C Barshilia and K. S. Rajam, Bull. Mater. Sci. **34 (3)**, 423 (2011).

[22] P. Chowdhury, B. Sellarajan, M. Krishnan, K. Raghuvaran, Harish. C. Barshilia, and K. S. Rajam, Adv. Sci. Lett. **4**, 1 (2012).

[23] M. J. Donahue, and D. G. Porter, OOMMF User's Guide, Version 1.0, Interagency report NISTIR 6376, National Institute of Standards and Technology, Gaithersburg, MD.

[24] K. R. Pirota, F. Béron, D. Zanchet, T. C. R. Rocha, D. Navas, J. Torrejon, M. Vazquez, and M. Knobel, J. Appl. Phys. **109**, 083919 (2011).

[25] D. Li, Richard S.Thompson, G. Bergmann, and Jia G. Lu, Adv. Mater **20**, 4575 (2008).

[26] R. Hertel, J. Magn. Magn. Mater. **249**, 251 (2002).

[27] F. Zighem, T. Maurer, F. Ott, and G. Chaboussant, J. Appl. Phys. **109**, 013910 (2011).